

Received 7 December 2020; revised 23 February 2021; accepted 25 February 2021. Date of publication 28 May 2021; date of current version 7 June 2021.

Digital Object Identifier 10.1109/OJAP.2021.3084842

Flat-Panel Mechanical Beam Steerable Array Antennas With In-Plane Rotations: Theory, Design and Low-Cost Implementation

QI TANG¹ (Member, IEEE), BART H. MCGUYER¹, ERIC BOOEN¹, SRISHTI SARASWAT¹, FARBOD TABATABAI¹, HAMID BOLANDHEMMAT¹, CURT VON BADINSKI¹, AND WILHELMUS H. THEUNISSEN^{1,2} (Senior Member, IEEE)

¹Facebook Inc., Menlo Park, CA 94025, USA

²SpaceX Co., Hawthorne, CA 90250, USA

CORRESPONDING AUTHOR: Q. TANG (e-mail: qitang@fb.com)

ABSTRACT We present a compact, flat-panel phased-array antenna design that beam steers using only mechanical in-plane rotations. We explain the steering mechanism and characterize the beam analytically and numerically. Measurements of two prototype antennas for different frequencies validate the concept and modeling. The prototype designs are described in detail and feature added phase-offset control of the array elements in the aperture layout. Potential applications include low-cost and low-power flat-panel user terminals for the next generation of aerial and space communication systems.

INDEX TERMS Beam steering, design-to-cost, flat-panel, high altitude platform, low earth orbit satellites, mechanical systems, moiré pattern, phased arrays, satellite ground stations, user terminals.

I. INTRODUCTION

MANY of the next-generation communication systems aiming to provide Internet access to un- or under-connected regions involve continuously moving terminals: satellites in low Earth orbit (LEO) or in medium Earth orbit (MEO) or high-altitude platforms (unmanned aerial vehicles or stratospheric balloons) [1], [2]. These systems require sophisticated ground-based user terminals that continuously track and frequently switch between the moving terminals. To maximize Internet access and be competitive with terrestrial solutions, these user terminals must be low cost, power efficient, and preferably compact [3]. However, despite recent progress, there are few if any commercial options that meet these challenging applications.

To date, the promising candidates for user and ground terminals include electronically steered arrays (ESAs) [4], [5], gimbal-steered antennas (GSAs), and mechanically steered arrays (MSAs) [6]–[12]. ESAs use active phase-shifter devices to control the phase of each array element, so are compact but power inefficient and expensive due to design complexity, fabrication cost, and commercial chip availability. GSAs use a mechanism to physically tilt the antenna in 3D, with or without additional electronic steering, so are

low power but bulky. MSAs use internal, mechanical reconfiguration, for example, in-plane rotations or displacements, to control the phasing of each array element and steer the beam. This allows a reduction in the degrees of freedom needed to steer the beam similar to that in a two-axis gimbal GSA, in contrast to a typical ESA with thousands of active phase shifters. Of the three candidates, MSAs have an attractive potential to combine the low power of a GSA, the compact form of an ESA, and a low cost. Examples of additional beam-steering techniques being researched include liquid crystal antennas, bifocal reflectarrays, and active metasurfaces [13]–[15].

One early type of MSA was the variable inclination continuous transverse stub (VICTS) antenna proposed in [6]. Since then, many variations have been developed for different frequencies [8]–[10]. Surprisingly, a clear explanation of the scanning mechanism of VICTS is usually not provided (except in [16]). In these MSAs, the in-plane rotation controls the incident angle of planar transverse electromagnetic (TEM) waves to steer the antenna beam. Another approach inspired by Risley prisms [11], [12] uses two phase-shifting surfaces (either dielectric lenses or metasurfaces). Their source wave propagates perpendicular to the phase-shifting

surfaces, requiring at least a few wavelengths of propagation distance that impacts the antenna height profile.

In this article, we use array factor theory to explain the beam scanning mechanism of a general class of MSAs. We propose a new design tool for MSAs by adding element phase control in the aperture layout design. In VICTS, a slow-wave parallel-plate wave guide (PPWG) is required to feed the half-wavelength-spaced radiating slots properly and prevent grating lobes [8]–[10]. Here, instead, we use PPWG built by machined stacked plates to prevent the expense of periodic grooves for slow wave structures and to reduce the loss from dielectric filling as used in VICTS. We built two full-aperture prototypes at different frequencies with two types of radiating elements: patch and single-arm spiral. We present measurements of the holographic field distribution on the aperture and the steering farfield radiation patterns at different rotation angles.

The article is organized as follows: Section II (Modeling) provides analytical and numerical modeling of MSAs in detail, treating our design as well as VICTS as a control, and addressing beam angle path, beam squint, dispersion, and aperture efficiency. Section III (Implementations) describes the detailed design of our two prototypes, including simulation of their collimators, radiating elements, and coupling structures. Section IV (Measurements) presents near-field holographic and far-field radiation pattern measurement results for our prototypes. The article ends with Section V (Summary).

II. MODELING

A. SETUP

The beam scanning mechanism of MSAs uses mechanical reconfigurations to change the phasing of all of the array elements, instead of using dedicated phase shifters for each array element as in ESAs. For the designs considered here, azimuth steering comes mainly from in-plane mechanical rotation of the antenna. Elevation steering, however, comes from a spatial interference pattern generated by a relative rotation between the array and a wave guide, which also perturbs the azimuth steering. This interference can be interpreted as an example of moiré phenomenon [17].

Figure 1 sketches the setup and features relevant to beam steering. Consider an M x N rectangular array of radiating elements. Let the S-plane rotate relative to the M-plane by a control angle ϕ_r as shown. For a transmitting antenna, the S-plane provides a feeding TEM wave in a PPWG. The amplitude and phase of each radiating element depends on exactly which region it samples from the S-plane beneath its position, which depends on ϕ_r . Together, the layout of the elements creates a discrete mask that samples different regions in the source S-plane. This sampling process is a multiplication of functions in the M- and S-planes and creates an interference pattern that depends on ϕ_r . The next sections calculate the elevation beam steering, its azimuth

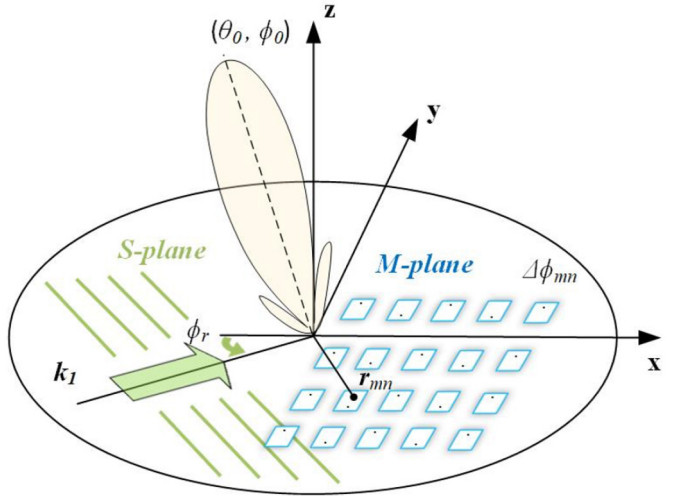


FIGURE 1. Mechanically steered antenna setup and the far field view above the antenna. The beam angles (θ_0, ϕ_0) are steered by both an in-plane rotation of the relative angle ϕ_r between the S- and M-planes to control mostly elevation angle θ_0 and a common rotation of both the S- and M-planes to control the azimuth angle ϕ_0 . The S-plane represents a source wave propagating along \hat{k}_1 . The M-plane represents a mask layer of radiating aperture with elements sampling the source wave at their locations \vec{r}_{mn} and with a fixed phase shift $\Delta\phi_{mn}$.

perturbation, and other performance factors analytically and numerically for our design as well as the VICTS. Without loss of generality, we will consider a transmitting antenna, but the results also apply for a receiving antenna.

B. ANALYTICAL MODELING

Consider an $M \times N$ rectangular array of radiating elements. Let each element be identical up to an intentional phase offset $\Delta\phi_{mn}$ that is fixed for each element, for example, by an in-plane rotation of their layout. The farfield radiation pattern is then the product of the pattern for each identical element and the array factor

$$F(\theta, \phi, \phi_r) = \sum_{n=1}^N \sum_{m=1}^M a_{mn}(\phi_r) e^{-jk\hat{r}(\theta, \phi) \cdot \vec{r}_{mn}}, \quad (1)$$

where the polar angle θ and azimuthal angle ϕ parameterize the far-field direction of radiation, the complex numbers $a_{mn} = |a_{mn}|e^{-j\psi_{mn}}$ characterize the excitation of each element by the feeding TEM wave, k is the free-space wave number for radiation, \hat{r} is the unit vector in the direction of (θ, ϕ) , and \vec{r}_{mn} is the vector position of each element.

The excitations $a_{mn}(\phi_r)$ parametrically depend on the relative rotation ϕ_r between the M- and S-planes. This rotation affects both the magnitude and phase of each excitation. However, for large-aperture antennas, the magnitude has to be roughly uniform to fully utilize the aperture. Therefore, we will approximate $|a_{mn}| \approx 1$ to simplify analytical modeling and compare with numerical results for $|a_{mn}| \neq 1$ below. With this approximation, the excitation phases are very nearly

$$\psi_{mn}(\phi_r) = k_1 x_{mn} \cos(\phi_r) + k_1 y_{mn} \sin(\phi_r) + \Delta\phi_{mn}, \quad (2)$$

where k_1 is the wave number of the feeding TEM wave. Importantly, these phases include the element offsets $\Delta\phi_{mn}$ that are controlled by the design.

To proceed, we will assume the element offsets have the linear form

$$\Delta\phi_{mn} = (m\alpha + n\beta)\pi \quad (3)$$

controlled by two fixed design parameters, α and $\beta \in [-1, 1]$, that set the phase variation per row and column of the array. For array positions $\vec{r}_{mn} = (md_x)\hat{x} + (nd_y)\hat{y}$ with fixed row and column spacings (d_x, d_y) , the array factor (1) becomes, after normalization,

$$F_1(\theta, \phi, \phi_r) = \frac{1}{MN} \left| \frac{\sin\left(\frac{M}{2}\Psi_m\right)}{\sin\left(\frac{1}{2}\Psi_m\right)} \right| \cdot \left| \frac{\sin\left(\frac{N}{2}\Psi_n\right)}{\sin\left(\frac{1}{2}\Psi_n\right)} \right|, \quad (4)$$

where the phases

$$\Psi_m(\theta, \phi, \phi_r) = (k \sin \theta \cos \phi + k_1 \cos \phi_r)d_x + \pi\alpha \quad (5)$$

$$\Psi_n(\theta, \phi, \phi_r) = (k \sin \theta \sin \phi + k_1 \sin \phi_r)d_y + \pi\beta. \quad (6)$$

The array factor $F_1(\theta, \phi, \phi_r)$ is periodic and has its local maxima when the phases Ψ_m and Ψ_n are integer multiples of 2π , each corresponding to a main or grating lobe in the farfield. Introducing integer indices p and $q \in \{0, \pm 1, \pm 2, \dots\}$ such that $\Psi_m = 2\pi p$ and $\Psi_n = 2\pi q$, the beam angles (θ_{pq}, ϕ_{pq}) of each (p, q) lobe then satisfy

$$\theta_{pq}(\phi_r) = \arcsin \left[\frac{(k_1 d_x \cos \phi_r + \pi\alpha - 2\pi p)^2}{(kd_x)^2} + \frac{(k_1 d_y \sin \phi_r + \pi\beta - 2\pi q)^2}{(kd_y)^2} \right]^{1/2} \quad (7)$$

$$\phi_{pq}(\phi_r) = \arctan \left[\frac{d_x (k_1 d_y \sin \phi_r + \pi\beta - 2\pi q)}{d_y (k_1 d_x \cos \phi_r + \pi\alpha - 2\pi p)} \right]. \quad (8)$$

Depending on the value of ϕ_r , the number of real-valued beam angles (θ_{pq}, ϕ_{pq}) will vary from none if there are no beams formed in the visible region to multiple if there are many main or grating lobes.

To proceed further, we must choose the design parameters d_x, d_y, α, β and potentially k_1 . The next sections do so for our prototype and the VICTS MSA. Many additional designs are possible and can be modeled with these design parameters.

C. PROTOTYPE MSAS

For this design, the element offsets are set by $\alpha = 1$ and $\beta = 0$ and the array positions by the spacings $d_x = d_y = \lambda_0/2$ where λ_0 is a central free-space wavelength for operation with wave number k . To reduce loss, there are no dielectrics inside the PPWG, so the wave number $k_1 = k$. The beam angles follow from Eq. (7)-(8) and are

$$\theta_{pq}(\phi_r) = \arcsin \left[\left(\cos \phi_r + \frac{k_0}{k} (1 - 2p) \right)^2 \right]$$

$$+ \left(\sin \phi_r - \frac{k_0}{k} (2q) \right)^2 \right]^{1/2} \quad (9)$$

$$\phi_{pq}(\phi_r) = \arctan \left[\frac{\sin \phi_r - k_0 (2q)/k}{\cos \phi_r + k_0 (1 - 2p)/k} \right]. \quad (10)$$

For operation at the central wavelength with $k_0 = k$, a main lobe exists while the control angle satisfies

$$\phi_r \in [-\pi/3 + r\pi, \pi/3 + r\pi] \text{ for integer } r \quad (11)$$

and correspond to $(p = 0 \text{ or } 1, q = 0)$. From the 180° rotational symmetry of the M-plane, the solution repeats for each choice of r , so we can choose $r = 0$ and $(p = 1, q = 0)$ without loss of generality. With this choice and the convention that the elevation angle is always positive, the beam angles for the main lobe simplify to

$$|\theta_0| = \arcsin |2 \sin(\phi_r/2)| \in [0, \pi/2] \quad (12)$$

$$\phi_0 = \begin{cases} (\phi_r - \pi)/2, & \phi_r \in (-\pi/3, 0], \\ (\phi_r + \pi)/2, & \phi_r \in [0, \pi/3). \end{cases} \quad (13)$$

The discontinuity in the azimuthal angle is an artifact of the choice to have a positive elevation angle. Equation 13 shows a linear relation of beam azimuth perturbation angle and control angle.

Figure 2 shows that beam angles from Eqs. (12)-(13) as ϕ_r rotates from -180° to 180° , with the M-plane fixed. The curves are colored to highlight the connection between the different plots. By rotating nearly $\pm 60^\circ$ about zero (or about $\pm 180^\circ$), the elevation angle is scanned from 0° to nearly 90° .

This ability to scan to such large elevation angles is important for applications with LEO satellites to maximize the duration of communication with each terminal. Note that the azimuthal angle is a linear correction from elevation steering. In an actual antenna with full two-dimensional (2D) beam control, a common rotation of both the M- and S-planes would be used to additionally steer azimuth, compensating as needed for this correction.

In Fig. 2, the antenna is able to steer exactly to zenith ($\theta_0 = 0^\circ$) for $\phi = 0, \pm\pi$. However, for frequencies away from the central frequency ($k_0 \neq k$), the antenna will not be able to steer within a keyhole region about zenith that grows with detuning, which will be treated numerically below. This occurs because steering to zenith requires a destructive interference that is sensitive to frequency [17].

D. VICTS MSA

Let us consider a scenario with the freedom of designing the wavenumber k_1 in the S-plane. For an example VICTS antenna, the element offsets are $\alpha = \beta = 0$. This antenna uses an array of linear slots instead of a rectangular array of discrete elements, so while the spacing $d_x = \lambda_0/2$, where λ_0 is the central wavelength, we will treat the other spacing with the continuous limit $d_y \rightarrow 0$. The feed has an ideal wavenumber $k_1 = 2k$ implemented with a PPWG filled with

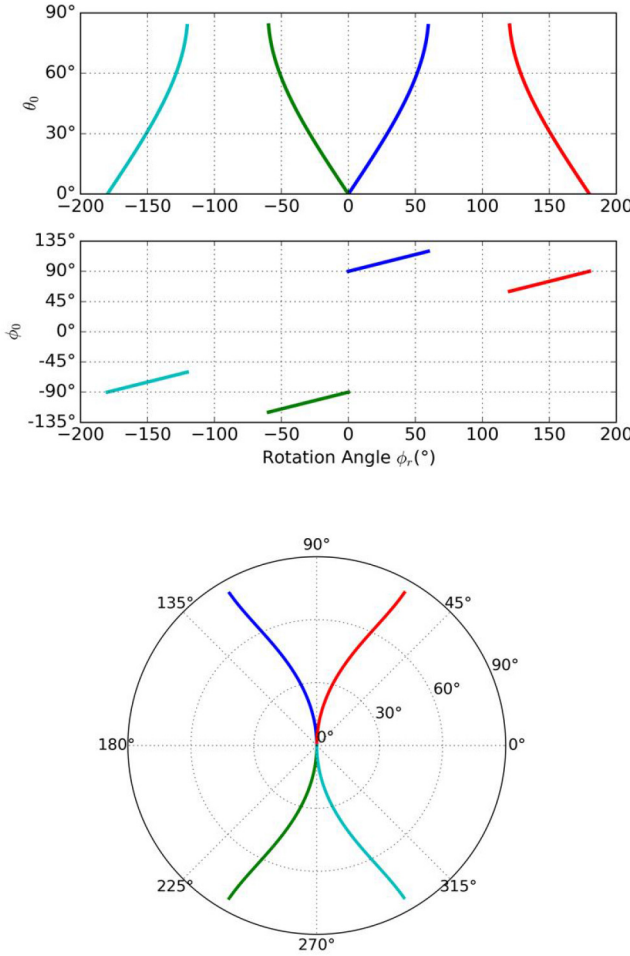


FIGURE 2. The angle path (θ_0, ϕ_0) of beam steering for the prototype MSAs as the feeding wave direction (ϕ_r) rotates from -180° to $+180^\circ$ in (top) linear and (bottom) polar coordinates. Here, the azimuth angle is a correction from elevation steering. In an actual antenna, a common rotation of both M- and S-planes would be used to additionally steer azimuth.

dielectric or a corrugated waveguide with an effective permittivity of 4. The beam angles follow from Eq. (7)-(8) and are

$$\theta_{pq}(\phi_r) = \arcsin \left[4(1 + p^2) - 8p \cos \phi_r \right]^{1/2} \quad (14)$$

$$\phi_{pq}(\phi_r) = \arctan \left[\frac{\sin \phi_r}{\cos \phi_r - p} \right]. \quad (15)$$

Fig. 3 shows the beam angles from Eq. (14)-(15) as θ_r rotates.

E. DISPERSION AND BEAM SQUINT

The beam steering of an MSA depends on a spatial interference between the feed wave number in the S-plane and one or both of the spacings used in the mechanical layout of the M-plane. As a result, for a fixed layout, the beam steering is sensitive to the feed wave number if it varies. We refer to the change in beam steering due to the wave number, all else equal, as the beam squint of the MSA. From Eqs. (9)-(10), the squint of our design depends on the relative bandwidth (RBW) but not the chosen operational frequency.

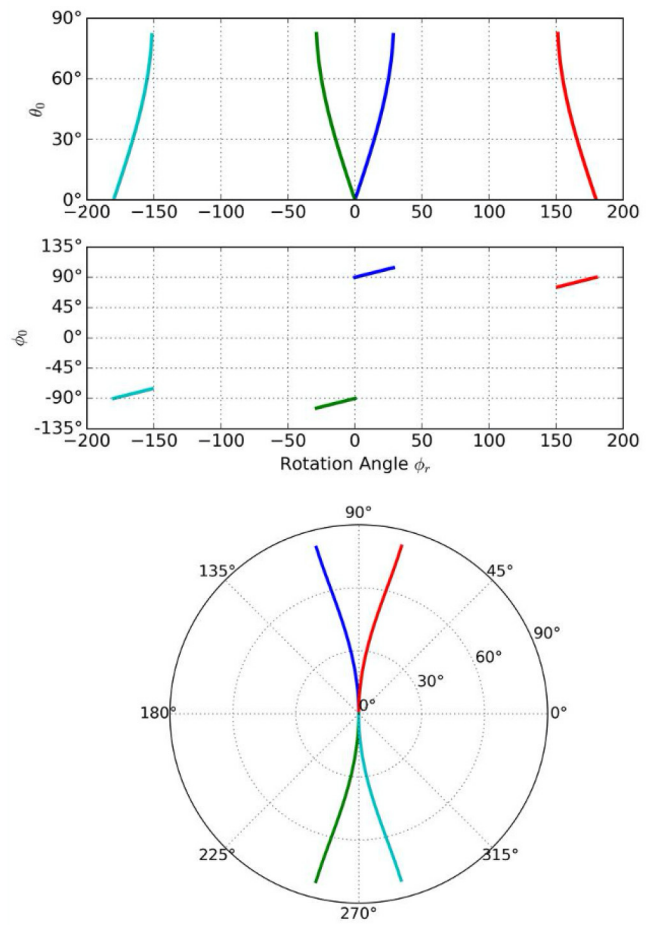


FIGURE 3. The angle path (θ_0, ϕ_0) of beam steering for the VICTS antenna as the feeding wave direction (ϕ_r) rotates from -180° to $+180^\circ$ in (top) linear and (bottom) polar coordinates. Here, as in Fig. 2, the azimuth angle is a correction from elevation steering. In VICTS antennas, a common rotation of both M- and S-planes is used to additionally steer azimuth.

Figure 4 shows the maximum beam squint of our prototype MSAs (and VICTS as a comparison) as a function of RBW and the control angle ϕ_r or equivalently, its elevation steering. The squint varies slightly with the control angle over most of its range, then significantly near 60° . The VICTS antenna shows a larger impact of squint effect at the same level of relative RBW as MSA due to its different design topology.

This beam squint is an important consideration for applications with large RBW. For example, if the frequencies are significantly different for transmit and receive, then it might be inefficient to combine both transmit and receive in the same aperture. Alternatively, separate transmit and receive MSAs could be used, or the M-plane could be modified to have two superposed arrays of elements, one for transmit and another for receive. Or, if the instantaneous RBW is narrow (e.g., 200 MHz) but a coverage over a wide operating RBW is desired, then the steering could be adjusted by proper design parameters, such as α and β , to correct for the beam squint for the instantaneous operating frequency.

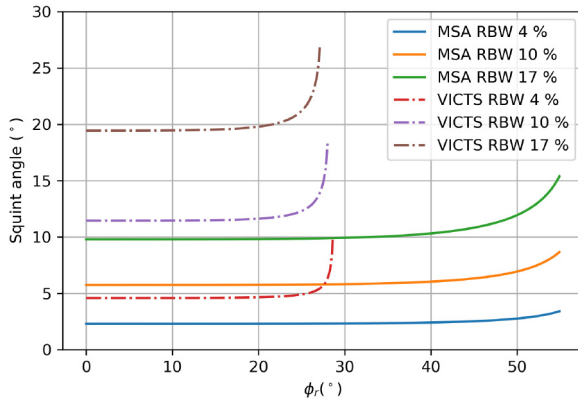


FIGURE 4. The maximum squint angle of the beam at different relative bandwidths for different rotations angles.

F. NUMERICAL MODELING

We used a Python code to numerically evaluate the array factor in Eq. (1) including more realistic design details, such as the layout shape and size as well as the amplitude variation of the element excitations, to estimate their impact on beam characteristics. Fig. 5 provides example calculations for a prototype MSA with a circular aperture with a diameter of 250 mm and an operating frequency of 14 GHz. It includes the farfield patterns in 2D azimuthal projection and the feed phase and amplitude distribution at each element. The numerical beam angles for the main lobe are consistent with the analytical solutions of (7)-(8), including the disappearance of a main lobe at $\phi_r = 80^\circ$. For the control angles shown, the beam path follows the upper left quadrant of Fig. 2 (bottom). The element positions are labeled with dots whose color and size indicate their relative excitation phase and amplitude. The amplitude distribution decays in the x-direction as the elements remove energy from the guide (as indicated by the decreasing size of the dots). Additionally, to approximate the TEM wave cross section in the guide, we applied a Gaussian amplitude tapering along the y-axis. One can see the change of phase and amplitude as the layout rotates. The phase pattern gains a periodicity with a spatial frequency that increases with rotation, or a tilt fringe, which generates the elevation angle steering.

G. APERTURE EFFICIENCY

The overall aperture efficiency for a finite-size MSA depends on many factors in both theory and practice. A typical high-directivity and low-sidelobe antenna requires a well-controlled uniform or tapered distribution of the excitation amplitudes of the radiating elements over the aperture. The coupling structure needs to be properly designed to well control the coupling efficiency which can be defined as the power delivered to the radiating element over the power propagating through and reflected from the feeding waveguide at one element spacing. If the feeding wave vanishes and only the first few columns of the array are excited, the

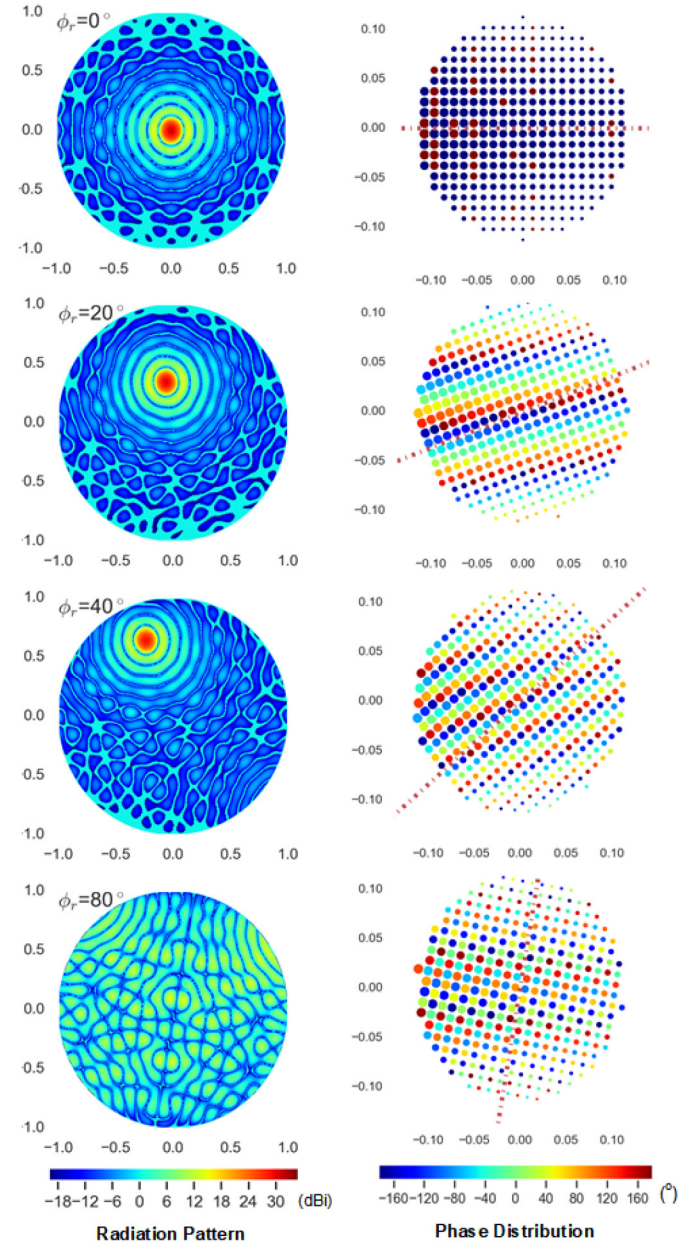


FIGURE 5. Simulated radiation patterns (left column) of MSA versus normalized wave number (directional cosines) and the changing phase and amplitude distribution of the element excitations (right column) versus position in meters as the aperture (M-plane) rotates counter-clockwise from 0° to 70° with the feeding wave (S-plane) fixed along the x-direction.

beam directivity and sidelobe rejection will degrade. In contrast, if the coupling efficiency is insufficient, most of the power will not couple to the elements but instead stay in the guide until termination, reducing the aperture efficiency. To analyze the impact of the loss at termination, we calculate an efficiency number η for a circular aperture diameter d_A antenna as

$$\eta = \int_{-d_A/2}^{d_A/2} \frac{1}{d_A} e^{-2k_1'' \sqrt{(d_A/2)^2 - y^2}} dy, \quad (16)$$

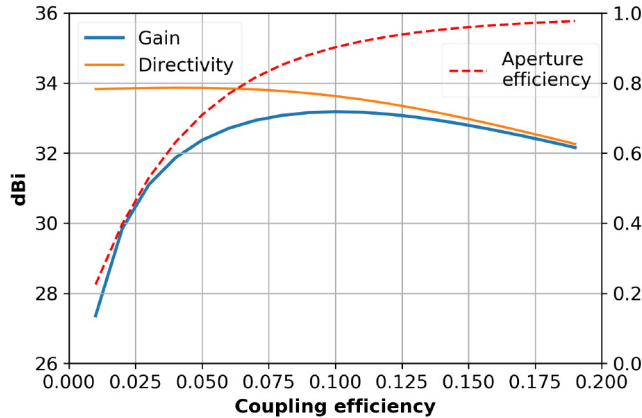


FIGURE 6. Design curves of the aperture gain, directivity, and aperture efficiency versus coupling efficiency with an aperture size of 350-mm diameter and an operating frequency of 14 GHz.

where $k_1'' = \text{Im}k_1$ is the attenuation constant of the feeding wave that relates to the coupling efficiency. The realized gain of MSAs $G = \eta D$, where D is the directivity which can be estimated by numerical modeling. The optimal choice of coupling efficiency for each element depends on the electrical size of the aperture, the desired beam pattern, and also the range of control-angle rotation needed for elevation-angle steering, because couplings optimized for one angle will generally not be optimized for all angles. For large aperture sizes, the difference tends to become negligible between an optimized coupling scheme giving uniform element excitation amplitudes and a uniform coupling scheme giving a decaying amplitude distribution. Therefore, we consider a uniform coupling for this and for the simplicity of its rotational symmetry for steering.

Figure 6 shows an example set of numerical design curves to optimize the aperture efficiency, directivity, and gain versus uniform element coupling efficiencies. The curves can be refined by applying a circular aperture with Gaussian TEM feed. The power efficiency drops quickly as the coupling efficiency decreases because most of the power is not radiated and dissipates at the guide termination. The directivity drops as the coupling factor increases because the beam quality degrades as the excitation amplitude becomes more nonuniform across the aperture. The optimal coupling factor is roughly 0.1 with a maximum gain of 33 dBi such that the resulting reflection at the element level is low, but sufficient power is extracted from the TEM wave. A range of coupling efficiency factors must be specified in the design procedure and the implemented value can be properly controlled by varying certain dimensions of the coupling structure. In practice, the overall aperture efficiency will also include power loss from dielectrics and metal in the waveguide, which are not included in Fig. 6.

III. IMPLEMENTATIONS

Satellite user terminals typically have separate spectra for uplink and downlink at different polarization state. For example, the transmit (uplink) antenna can operate

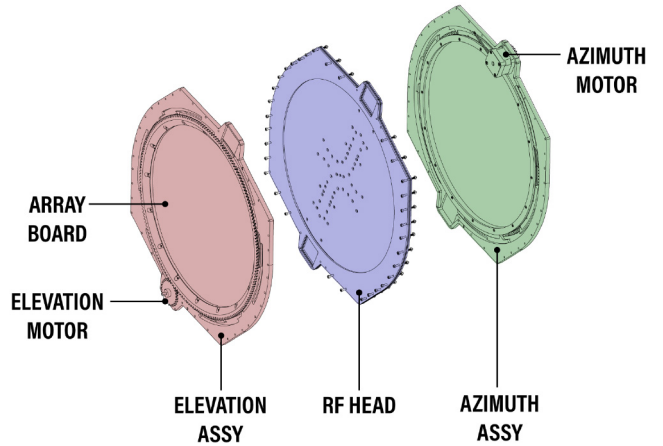


FIGURE 7. Mechanical assembly of the prototype MSAs showing the S-plane (array board), M-plane (RF head), and two motors for full 2D steering.

at 14–14.5 GHz with a left hand circular polarization (LHCP) and the receive (downlink) antenna operates at 10.7–12.7 GHz with a right hand circular polarization (RHCP). We design two separate MSA apertures for uplink and downlink, and mainly focus on the transmit antenna as a proof of concept.

Fig. 7 illustrates the mechanical assembly of these MSA prototypes. Each consists of an array board (S-plane), a collimating waveguide structure (M-plane, or RF head), and a base (azimuth assembly). The array board contains a motor that drives its rotation for elevation steering, and the azimuth assembly contains a motor that drives both S- and M-plane rotation for azimuth steering.

A. COLLIMATING STRUCTURE

We approximate an ideal traveling TEM wave in the S-plane with a collimated beam in a finite waveguide [18]. This beam is generated by a two-level structure, known as a parabolic folded pillbox [19]. The beam is fed by a planar horn at the focal point of a parabolic reflector on a bottom layer, which creates a collimated beam on the upper layer. The upper layer is a guide that serves as the S-plane. The slot transition that transfers energy between the upper and lower layers needs careful design to minimize insertion and reflection loss. In our design, we have a second reflector and horn to capture the outgoing, non-radiated beam, though a terminating structure can also be used. Having two horns adds an additional control degree of freedom of switching the direction of the beam in the S-plane guide by 180° without mechanical rotation. Additionally, the two horns provide two ports for characterizing the collimator performance, estimating its wave front quality, and thus estimating its radiating efficiency.

Figure 8 shows the collimator design and the simulated field distributions in the lower and upper layers. The simulation is conducted with a commercial full-wave numerical simulation software (Ansys HFSS). The planar feed horns are offset positioned and the waveguides are bent to fit

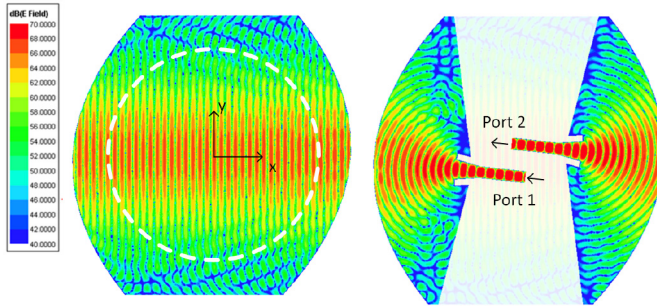


FIGURE 8. Collimator design and simulated field distributions in the layers above and below the RF head in Fig. 7, showing the beam collimation beneath the array board.

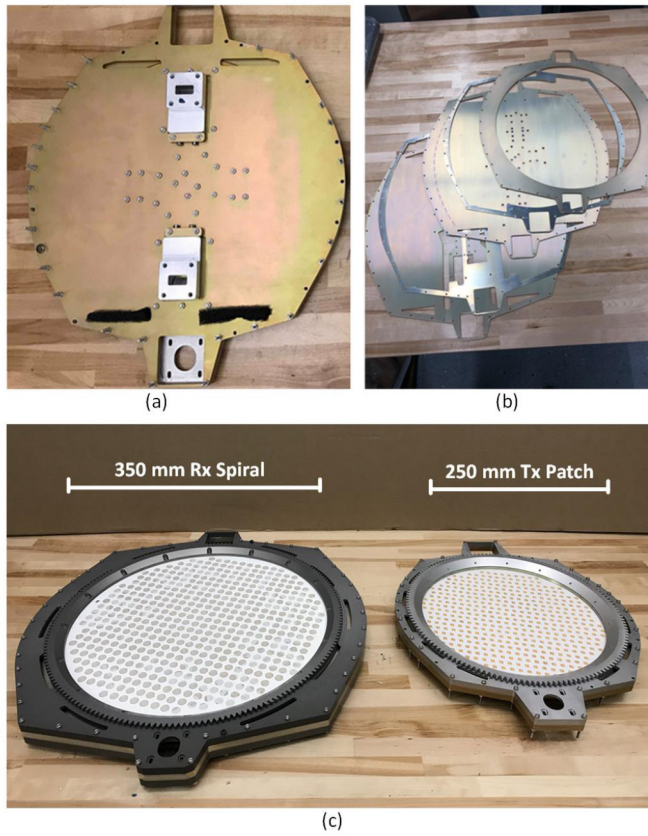


FIGURE 9. (Top) Pictures of the collimating cavity (RF head) built from machined stacked plates with design to cost; (Bottom) Picture of the assembled MSAs with two radiating array board designs including (left) a 350 mm-diameter receive antenna operating at 10.7–12.7 GHz and (right) a 250 mm transmit antenna operating at 14–14.5 GHz.

the mechanical assembly. The layers are made of stacks of machined aluminum plates. To minimize cost, standard plate thicknesses were used which allowed low-cost laser and waterjet cutting. The guide heights are set by standardized aluminum sheet thicknesses (64 mil).

B. RADIATING BOARD

The M-plane is implemented by a radiating array board with ground plane that is mounted on top of the upper layer. To apply the relative-rotation control angle, a rotation joint was

designed to support the mechanical rotation of the board while preventing RF leakage. To minimize leakage, an RF choke was designed around the edge of the board near the joint bearing, allowing enough mechanical separation for friction free rotation without significant RF loss. We limit the number of layers in the substrate stack-up for lower cost and complexity. The radiating board is fabricated with low-loss Isola100G raw material. The dielectric constant is 3.1 and loss tangent is 0.002.

C. RADIATING ELEMENTS

The radiating elements in the M-plane array board had a rectangular array layout with half-wavelength spacing to suppress grating lobes. The intentional element phase offsets set by $\alpha = 1, \beta = 0$ were implemented with a 180° phase shift between each row that came from alternating the layouts of the elements or their coupling structures between rows, as described below.

We investigated two types of structures in the element design as shown in Fig. 10: (i) an offset single-feed truncated patch and (ii) a single-arm spiral element. Both are circularly polarized. The single-arm spiral element has advantages in greater bandwidth and rotational insensitivity, but a disadvantage of a radiation pattern that tilts with substrate thickness. Simulation were conducted to design both types of the elements. The cavity thickness is 64mil. The board thickness is 128mil with 2-layer stack-ups of 32mil and 96mil in the bottom and top layer. The through via diameter is 20mil and cavity via diameter is 10mil. The element spacing is 10.5 mm for 250 mm Tx aperture and 12.5 mm for 350 mm Rx aperture.

Fig. 11 presents the simulation results of the LHCP and RHCP gain for a truncated patch element design operating from 14 to 14.5 GHz and a single-arm spiral element design working from 10.7 to 12.7 GHz. The in-band input matching results are also shown, and were around -15 dB with a 50 Ohm signal input port defined at the via feed position on the ground plane. As aperture size increases, board warpage can be a dominant factor impacting on the coupling efficiency and beam quality in the upper layer guide.

D. COUPLING STRUCTURES

The coupling structures that connect the radiating elements in the M-plane radiating board and the feeding wave in the S-plane guide are important to minimize perturbation of the feeding wave. We chose pins and ring slots for these structures. Pins can properly control the coupling efficiency by changing their insertion distance into the upper cavity. However, pins also introduce a lot of challenges in practice. For example, metallic pins have substantial weight that can deform the radiating board near its center and pin length needs to be adjusted causing challenges in the mechanical design and assembly. Coupling slots integrated into the radiating board offer more potential to reduce the total cost and complexity of assembly for large volume manufacturing.

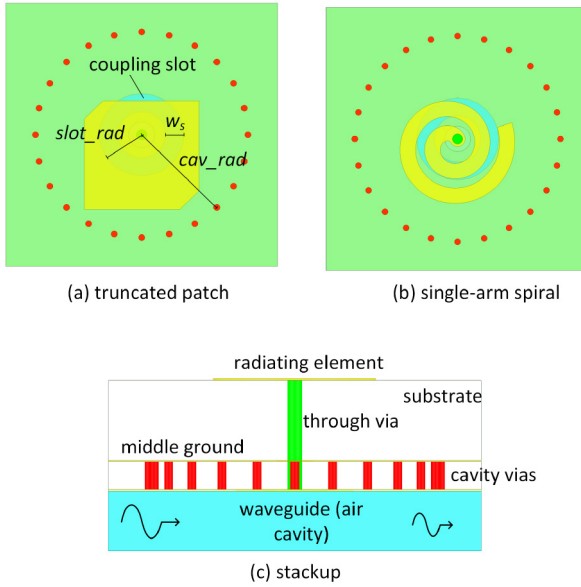


FIGURE 10. A front view of (a) a truncated patch element and (b) a single-arm spiral element, and a side view of (c) the vertical stackup of the radiating element, coupling structure and upper waveguide cavity. The key design parameters of the coupling structure for controlling the coupling efficiency are labeled here, including the slot radius (*slot_rad*), slot width (*w_s*) and cavity radius (*cav_rad*).

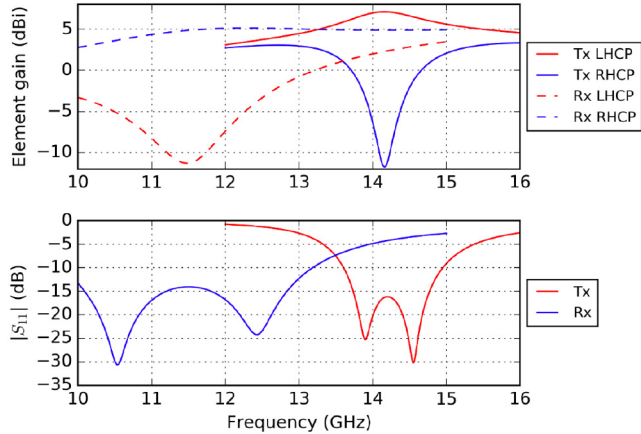


FIGURE 11. (Top) Simulated LHCP and RHCP gain of a truncated patch element in the $\phi = 0^\circ$ plane. (Bottom) Input reflection coefficient (S_{11}) as a function of frequency.

Figure 10 depicts the vertical profile of the ring slot coupling structure. A ground layer and via cavity isolate the coupling structure and the radiating element. We use commercial software to run a full-wave simulation of the ring slot coupling structure integrated with radiating elements and feeding waveguide. Figure 12 shows a controllable coupling efficiency by tuning the design parameter *slot_rad*. The coupling efficiency is defined by the ratio of radiated power over the total input power which can be approximately estimated by $1 - |S_{21}|^2 - |S_{11}|^2$, where S_{11} and S_{21} are the reflection and transmission coefficient of one unit cell. Our study shows there is a design trade-off between increasing the coupling efficiency and minimizing perturbation on the feed beam in the PPWG. The design also needs to minimize the reflection

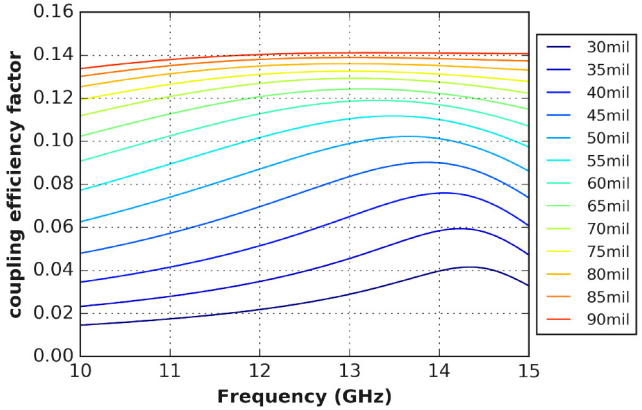


FIGURE 12. Coupling factor curves versus the design parameter *slot_rad* while $w_s = 15\text{ mil}$ and $cav_rad = 170\text{ mil}$.

coefficient to minimize inter-element multiple reflection. A ring slot is essentially a resonant structure to maximize its coupling between cavities. Last but not least, the design of the coupling structure needs to keep its coupling efficiency stable across the full bandwidth.

To control the intentional phase offsets, the pins layout was rotated within the layout of individual elements for the truncated patches, and the in-plane rotation of individual elements was adjusted for the spiral arm radiating elements.

IV. MEASUREMENTS

We fabricated and assembled two prototype circular-aperture MSAs with the element designs discussed in Section III. One MSA used truncated patch elements with an aperture diameter of 250 mm. The other MSA used spiral element with a diameter of 350 mm. Antenna radiation patterns were measured with a near-field scanner as shown in Figs. 13–15. We present measurement results from the transmit 250 mm antenna.

Raw data points of near field patterns were collected at different rotation angles. Holograms of the field distributions on top of the aperture surface were post-processed and visualized. Figure 13 shows an example of the patch aperture at a rotation angle of 0° and 37° and a frequency of 14.5 GHz at 0.25 GHz offset from the center frequency (designated for half wavelength element spacing). One can visualize a clean circular aperture in the amplitude heatmap showing the radiating elements as expected. A decaying amplitude inside the aperture along the x-direction which indicates the element coupling structure works as expected. Figure 13(a) shows a closed-to-uniform phase distribution across the aperture at 0° rotation angle with a slight tilt due to the frequency offset. In the case of 37° rotation, the phase is linearly progressing at a specific oblique angle and periodicity correlating to the azimuth and elevation angle of the farfield beam direction.

The measured farfield radiation patterns are also presented in Fig. 13 showing a clean mainlobe in the boresight direction at 0° rotation and a tilted beam at 37° rotation. The axial ratio of polarizations was manually checked to be less than 6 dB

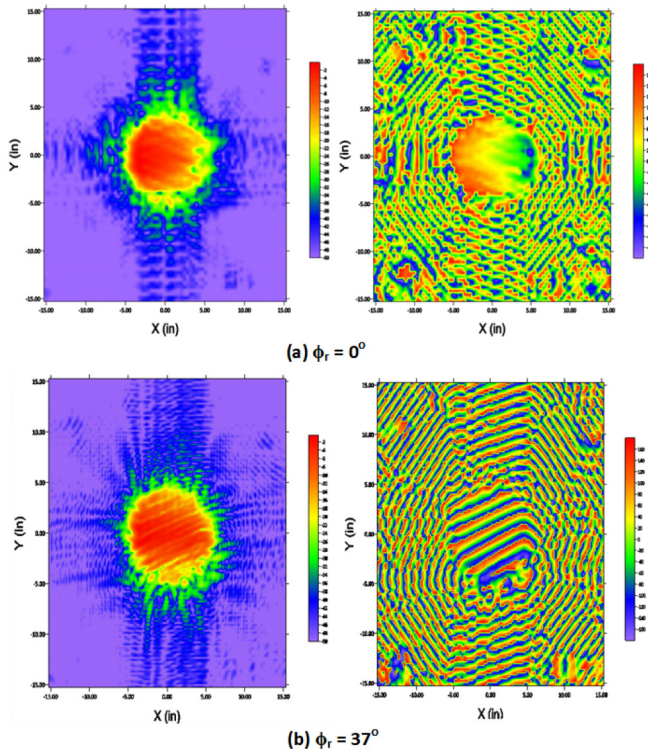


FIGURE 13. Holographic field amplitude (left) and phase (right) distribution measurements on the surface plane of the transmit truncated patch aperture at 14.5 GHz for two rotation angles: (a) $\phi_r = 0^\circ$ and (b) $\phi_r = 37^\circ$.

over the 14–14.5 GHz band, which can be further improved by tuning the element geometry and aperture layout. Azimuth and elevation tilt angles work as expected with a progressive phase shift along the aperture at different angles as expected by modeling.

One-dimensional (1D) cuts of the measured beam directivity patterns for the patch element aperture design is normalized and shown in Fig. 14 with different rotation angles from 0 to 45° . The measured beam angles are consistent with the prediction of analytical and numerical solutions in Section II. The absolute maximum gain measured in the Tx aperture is given in Fig. 15 also shown with different rotation angles. We achieved an aperture efficiency of about 15–37% compared to the theoretical limit of 80–90% in Fig. 6. The loss may come from the different parts of the system, including the waveguide loss, the transition loss between upper and lower cavity coupling, and most importantly the degradation of beam directivity due to the element coupling efficiency control and the cleanliness of TEM waveform. We use the maximum gain of the main lobe as a key performance indicator of the cleanliness of the antenna radiation pattern. The maximum directivity of the measurement results are close to the theoretical predictions with a discrepancy coming from the amplitude tapering of the collimated beam in the cross-section.

Challenges remain on controlling and maintaining proper and constant coupling efficiency across the frequency band

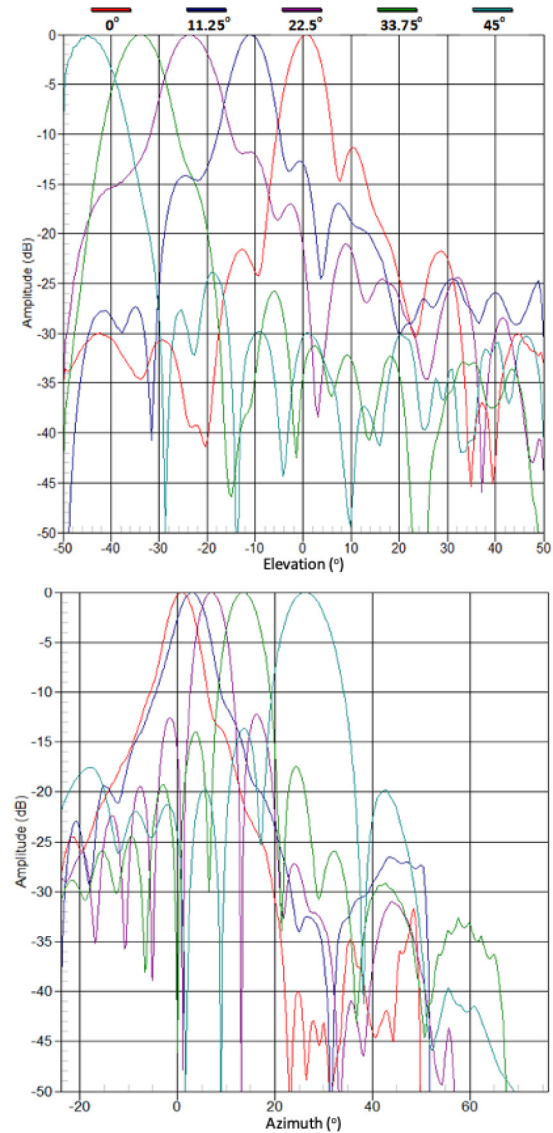


FIGURE 14. Orthogonal 1D cuts of the measured radiation patterns at different rotation angles.

for optimal aperture gain and gain stability. We've also observed varying gain across different incident angles which can be suppressed by further optimization of the aperture layout. Last but not the least, for satellite applications, there is a need to optimize the mechanical control and the feed-port switching to minimize the hand-over switching time between different satellites.

V. SUMMARY

In this article, we derive analytical solutions for and analyze the beam characteristics of a general class of MSAs in detail. We use a new design degree of freedom with element phase offsets to simplify the S-plane waveguide implementation compared to a VICTS. We report on two prototypes that use spiral or patch elements and demonstrate beam steering. The prototype designs focus on lowering cost through

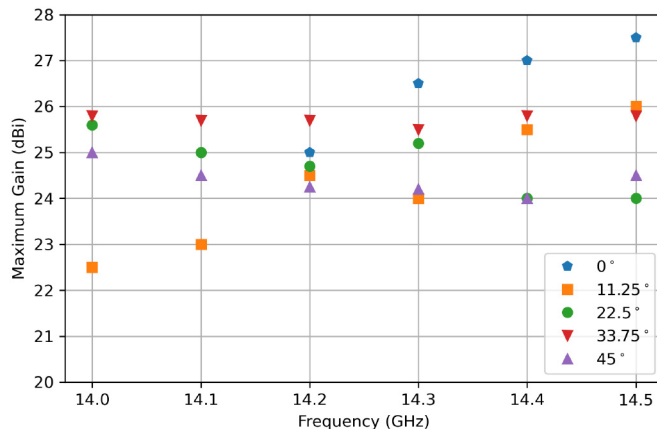


FIGURE 15. The measured maximum gain of the radiation pattern for the 250mm Tx truncated patch aperture as a function of frequencies with different cases of rotation angles.

minimizing machining and integrating their coupling slots. We present measurements of field distributions, beam patterns, and maximum gains at different rotation angles. Future work could improve the beam characteristics and steering performance, including aperture efficiency, gain stability, and side-lobe suppression. This work demonstrates the potentials and challenges in MSA design for flat-panel ground terminals in aerial and space communication or other applications such as 5G networks.

ACKNOWLEDGMENT

The authors greatly thank Jin Bains for his support of this work. All work was performed by Facebook Inc.

REFERENCES

- [1] I. del Portillo, B. G. Cameron, and E. F. Crawley, “A technical comparison of three low earth orbit satellite constellation systems to provide global broadband,” *Acta Astronautica*, vol. 159, pp. 123–135, Jun. 2019.
- [2] Q. Tang *et al.*, “Demonstration of a 40gbps bi-directional air-to-ground millimeter wave communication link,” in *Proc. IEEE MTT-S Int. Microw. Symp. (IMS)*, 2019, pp. 746–749.
- [3] I. del Portillo, “Space and aerial architectures to expand global connectivity,” Ph.D. dissertation, Dept. Aeronaut. Astronaut., Massachusetts Inst. Technol., Cambridge, MA, USA, December 2019.
- [4] M. Stoneback and K. Madsen, “A planar all-silicon 256-element Ka-band phased array for high-altitude platforms (HAPs) application,” in *Proc. IEEE/MTT-S Int. Microw. Symp.*, 2018, pp. 783–786.
- [5] W. Theunissen, V. Jain, and G. Menon, “Development of a receive phased array antenna for high altitude platform stations using integrated beamformer modules,” in *Proc. IEEE/MTT-S Int. Microw. Symp.*, 2018, pp. 779–782.
- [6] W. Milroy, “The continuous transverse stub (CTS) array: Basic theory experiment and application,” in *Proc. Antenna Appl. Symp.*, vol. 2, 1991, pp. 253–283.
- [7] D. F. Sievenpiper, J. H. Schaffner, H. J. Song, R. Y. Loo, and G. Tangonan, “Two-dimensional beam steering using an electrically tunable impedance surface,” *IEEE Trans. Antennas Propag.*, vol. 51, no. 10, pp. 2713–2722, Oct. 2003.
- [8] T. Sikina, D. McKay, K. Komisarek, and B. Porter, “Variably inclined continuous transverse stub-2 antenna,” in *Proc. IEEE Int. Symp. Phased Array Syst. Technol.*, 2003, pp. 435–440.
- [9] M. Ettorre, F. F. Manzillo, M. Casaletti, R. Sauleau, L. Le Coq, and N. Capet, “Continuous transverse stub array for Ka-band applications,” *IEEE Trans. Antennas Propag.*, vol. 63, no. 11, pp. 4792–4800, Nov. 2015.
- [10] T. Potelon *et al.*, “A low-profile broadband 32-slot continuous transverse stub array for backhaul applications in E-band,” *IEEE Trans. Antennas Propag.*, vol. 65, no. 12, pp. 6307–6316, Dec. 2017.
- [11] A. A. Baba, R. M. Hashmi, K. P. Esselle, M. Attygalle, and D. Borg, “A millimeter-wave antenna system for wideband 2-D beam steering,” *IEEE Trans. Antennas Propag.*, vol. 68, no. 5, pp. 3453–3464, May 2020.
- [12] X. Zhao, C. Yuan, J. Zhang, and Q. Zhang, “Design of a beam scanning metamaterial antenna with polarization transform for high-power microwave application,” *Microw. Opt. Technol. Lett.*, vol. 62, no. 10, pp. 3255–3265, 2020.
- [13] R. Jakoby, A. Gaebler, and C. Weickmann, “Microwave liquid crystal enabling technology for electronically steerable antennas in SATCOM and 5G millimeter-wave systems,” *Crystals*, vol. 10, no. 6, p. 514, 2020.
- [14] P. Nayeri, F. Yang, and A. Z. Elsherbeni, “Bifocal design and aperture phase optimizations of reflectarray antennas for wide-angle beam scanning performance,” *IEEE Trans. Antennas Propag.*, vol. 61, no. 9, pp. 4588–4597, Sep. 2013.
- [15] B. Ratni *et al.*, “Gradient phase partially reflecting surfaces for beam steering in microwave antennas,” *Opt. Exp.*, vol. 26, no. 6, pp. 6724–6738, 2018.
- [16] B. G. Porter, “Closed form expression for antenna patterns of the variable inclination continuous transverse stub,” in *Proc. IEEE Int. Symp. Phased Array Syst. Technol.*, 2010, pp. 164–169.
- [17] B. H. McGuyer and Q. Tang, “Connection between antennas, beam steering, and the moiré effect,” to be published.
- [18] E. Boonen and W. H. Theunissen, “Collimated transverse electric mode cavity antenna assembly,” U.S. Patent 10 367 255, Jul. 2019.
- [19] Y. T. Lo and S. Lee, *Antenna Handbook: Volume III Applications*. New York, NY, USA: Springer, 2012. [Online]. Available: https://www.google.com/books/edition/Antenna_Handbook/_0wOBwAAQBAJ?hl=en&gbpv=1